

Global prevalence of compound heatwaves from 1980 to 2022

Kun ZHANG^{a,b,c}, Jin-Bao LI^d, Michael Kwok-Po NG^{e,*}, Zheng-Fei GUO^{b,c}, Amos P.K. TAI^{f,g,h}, Shu-Wen LIU^{b,c}, Xiao-Rong WANG^{b,c}, Jie ZHANG^{b,c}, Jin WU^{b,c,g,**}

^a School of Geospatial Engineering and Science, Sun Yat-sen University, Zhuhai 519082, China

^b School of Biological Sciences, The University of Hong Kong, Hong Kong 999077, China

^c Institute for Climate and Carbon Neutrality, The University of Hong Kong, Hong Kong 999077, China

^d Department of Geography, The University of Hong Kong, Hong Kong, 999077 China

^e Department of Mathematics, Hong Kong Baptist University, Hong Kong, 999077 China

^f Department of Earth and Environmental Sciences, Faculty of Science, The Chinese University of Hong Kong, Hong Kong 999077, China

^g State Key Laboratory of Agrobiotechnology, The Chinese University of Hong Kong, Hong Kong 999077, China

^h Institute of Environment, Energy and Sustainability, The Chinese University of Hong Kong, Hong Kong 999077, China

Received 28 October 2024; revised 8 April 2025; accepted 17 April 2025

Abstract

Global warming has led to increasing occurrence of hot extremes, yet our understanding of the compound heatwaves (CHW) of both day and night—the most threatening and harmful type—remains limited. Here we use the air temperature from ERA5-Land datasets to analyze key characteristics of global CHW from 1980 to 2022. Our results demonstrate a pronounced increase in global CHW, with an annual cumulative intensity rising by 3.32 °C per decade ($p < 0.001$), approximately four times greater than the increases observed in individual heatwave types of daytime (0.73 °C per decade, $p < 0.001$) and nighttime (0.78 °C per decade, $p < 0.001$), respectively. High latitudes in the Northern Hemisphere, particularly the Arctic regions, have experienced the highest increases in CHW (>10 °C per decade), especially since 2005. Moreover, inter-annual variations of CHW are closely linked to major climate modes, displaying strong region-specific connections and varied lagged effect, particularly with ENSO and PDO in tropical regions. Altogether, these results reveal the unexpected prevalence of CHW in recent decades, emphasizing the urgent need to address its potential adverse impacts on human and ecosystem well-being.

Keywords: Compound heatwaves; Climate mode; Global pattern; Temporal dynamics

1. Introduction

Heatwaves, a critical type of climate extreme, are characterized by abnormally and persistently high temperatures near the Earth's surface (Russo et al., 2015). Growing studies indicate that heatwaves have become more frequent and severe in recent

decades due to global warming (Fischer et al., 2021; Luo and Lau, 2021; Yuan et al., 2023), posing substantial risks to human health and ecosystems primarily by causing heat stress (Liao et al., 2024; Perkins-Kirkpatrick et al., 2024; Yang et al., 2024). Moreover, heatwaves adversely impact the natural environment through various mechanisms, such as decreased ecosystem productivity (Brás et al., 2021; Ciais et al., 2005), increased tree mortality (Anderegg et al., 2013), disrupted land–atmosphere energy exchange (Li et al., 2021), and heightened wildfire frequency and intensity (Park Williams et al., 2013). These effects, in turn, threaten the overall structure and function of terrestrial ecosystems (Teuling et al., 2010).

Early studies on heatwaves primarily focused on the abnormality of daytime maximum temperature, without

* Corresponding author.

** Corresponding author. School of Biological Sciences, The University of Hong Kong, Hong Kong 999077, China.

E-mail addresses: michael-ng@hku.edu.hk (NG M.K.-P.), jinwu@hku.hk (WU J.).

Peer review under responsibility of National Climate Centre (China Meteorological Administration)

differentiating nighttime temperature conditions (Perkins et al., 2015; Reddy et al., 2022; Russo et al., 2014). Recent studies (Chen and Zhai, 2017; Luo et al., 2022; Wang et al., 2020a) have considered explicitly both daily maximum (T_{\max}) and minimum (T_{\min}) temperatures, leading to the distinction between daytime heatwaves (DHW), characterized by anomalously high T_{\max} , and nighttime heatwaves (NHW), characterized by anomalously high T_{\min} . This distinction has allowed for the recognition of a special type of heatwave known as compound heatwaves (CHW), which are marked by persistent hot extremes during both daytime and nighttime. Unlike individual daytime or nighttime heatwaves, CHW is particularly detrimental to human and ecosystem health as they inhibit recovery from heat stress experienced in prior episodes (Fischer and Schär, 2010; Wang et al., 2020b). Furthermore, CHW is often associated with hot-humid conditions and more complex formation processes, which lead to higher temperature extremes (Baldwin et al., 2019) and severe heat-induced consequences to both human society and natural ecosystems (Wang et al., 2020a; Zhao et al., 2023; Zhou et al., 2025).

However, current studies have predominantly focused on using individual T_{\max} thresholds to track heatwave changes. For instance, when considering only the T_{\max} threshold, the frequency of heatwaves exerts a greater influence on heat accumulation compared to the intensity of heatwaves (Perkins-Kirkpatrick and Lewis, 2020). Only a few studies dedicated to quantifying the distinct patterns of DHW, NHW, and CHW, and investigating the underlying characteristics of various types of heatwaves (Luo et al., 2022; Wu et al., 2023). Even fewer examined their potential impacts on human health and population exposure under future socioeconomic pathway scenarios (Ma et al., 2022; Wang et al., 2021). Nevertheless, on a global scale, a comprehensive understanding of the spatiotemporal pattern of CHW remains lacking. In particular, knowledge gaps persist regarding how CHW varies relative to individual heatwave types (DHW and NHW), thereby limiting the capacity to comprehensively evaluate the CHW-related impacts and mitigation strategies.

Moreover, increasing air temperatures, which serve as a direct cause of local hot extremes, have been linked to the weakened advection of warm air flow due to atmospheric blocking patterns (Schaller et al., 2018). These patterns are often influenced remotely by atmospheric circulation modes through dynamical teleconnections (Alexander et al., 2002; Luo and Lau, 2020; Ma et al., 2024; Parker et al., 2014). Consequently, determining the cause and enhancing the predictability of heatwaves depend on our understanding of their associations with internal climate modes. Despite some studies have examined the relationship between regional heatwaves and specific teleconnection patterns (Liang et al., 2023; Perkins et al., 2015; Reddy et al., 2022), the time-dependent connections between CHW and various modes of climate variability on a global scale remain unexplored.

This study will systematically evaluate the global spatiotemporal pattern of CHW and explore potential connections between regional CHW variations and major global climate

variability modes. Specifically, we aim to address the following scientific questions: 1) What are the spatiotemporal patterns of CHW frequency and intensity globally in recent decades, and how do these characteristics differ from those of individual-type heatwaves? 2) Which climate variability modes are potentially associated with the observed CHW patterns, and what are the regional and time-series characteristics of these associations? These findings will deepen understanding of global CHW dynamics and provide critical insights to policymakers for developing climate mitigation strategies and early warning systems.

2. Materials and methods

2.1. Data

We used the 2 m air temperature data from the fifth generation of European reanalysis data (ERA5-Land, hereafter referred to as ERA5L, Hersbach et al., 2020) to estimate global terrestrial heatwaves over the past 43 years (1980–2022) at a spatial resolution of 0.1°. The maximum and minimum daily temperatures (T_{\max} and T_{\min}) derived from the ERA5L were employed to detect global heatwaves, and the original air temperature observations from ERA5L are available at <https://doi.org/10.24381/cds.e2161bac>.

To further ensure the credibility of our heatwave estimates, we also incorporated two additional global air temperature datasets: the Modern-Era Retrospective analysis for Research and Applications, Version 2 (MERRA2, <https://doi.org/10.5067/SUQESM06LPK>), provided by NASA (Gelaro et al., 2017), and the second Japanese global atmospheric reanalysis product (JRA55, <http://search.diasjp.net/en/dataset/JRA55>) constructed by the Japan Meteorological Agency (Kobayashi et al., 2015). MERRA2 and JRA55 are widely used global reanalysis products with temporal resolutions of 3 and 6 h, and spatial resolutions of 0.5° × 0.625° and 1.25° × 1.25°, respectively. For these datasets, we firstly calculated the corresponding daily T_{\max} and T_{\min} values, and then used the derived metrics for subsequent heatwave detection.

In addition, we accessed the 16 modes of climate variability obtained from two prominent sources: the Physical Sciences Laboratory (PSL) of the National Oceanic and Atmospheric Administration (NOAA, https://psl.noaa.gov/data/climate_indices/), and the Climate Explorer of the Royal Meteorological Institute of the Netherlands (KNMI, <https://climexp.knmi.nl/>). These modes can be categorized according to their anomalous sea surface temperature (SST) and atmospheric pressure characteristics. A comprehensive summary of these modes is provided in Table A1 for reference.

2.2. Heatwave detection

The principle underlying heatwave detection relies on identifying hot temperature anomalies in each grid cell, compared to their respective historical temperature variation ranges. First, we calculated a hot threshold to ascertain

whether the temperature for a selected grid on a specific date is sufficiently high. Generally, the hot threshold can be derived at a particular percentile over a reference period. To achieve this, we considered the union sets of temperatures (X_d) for each grid at a given date within a 31-d time window over the reference period (1981–2010), as illustrated in Eq. (1):

$$X_d = \bigcup_{y=1981}^{2010} \bigcup_{d-15}^{d+15} T_{y,d} \quad (1)$$

where \cup denotes the union of sets, T refers to the time series of air temperatures for each grid, and d and y denote the given day and specific year, respectively. Consequently, the hot threshold for each grid at a given day can be determined using the empirical cumulative distribution function (eCDF) at the 90th percentile of X_d . Subsequently, the hot threshold (Fig. 1) for daily maximum and minimum temperature (*i.e.*, designated as $C_{90\max}$ and $C_{90\min}$ for T_{\max} and T_{\min} , respectively) can be employed to estimate compound heatwaves ($T_{\max} > C_{90\max}$ and $T_{\min} > C_{90\min}$), daytime heatwave ($T_{\max} > C_{90\max}$ and $T_{\min} < C_{90\min}$), and nighttime of heatwaves ($T_{\max} < C_{90\max}$ and $T_{\min} > C_{90\min}$), separately (Fig. 1b).

Following the above steps for identifying the abnormally hot daily temperatures, we proceeded to automatically connect all neighboring heatwave candidates, and only retained those realized heatwaves that persisted for at least three consecutive days, in accordance with previous studies (Luo et al., 2022; Russo et al., 2015). Consequently, the daily heatwave intensity (I_{3d}) can be quantified as the surplus temperatures ($T_{\max\min_extra}$) based on the hot threshold (C_{90}), while also satisfying the temporal filter of three consecutive days (Eq. (2)). Finally, we repeated these steps for all grids across the global land surface, enabling the detection for different types of heatwaves throughout the examined data time series.

$$I_{3d} = \max |(T_a - C_{90}, 0)|_{\geq 3d} \quad (2)$$

This study employs three key metrics to evaluate annual heatwaves: 1) the annual frequency of heatwaves (HWF), determined by summing all heatwave days throughout the year; 2) the annual cumulative intensity of heatwaves (HWCI), which represents the sum of daily heatwave intensity values

over the entire year; and 3) the annual mean intensity of heatwaves (HWI), yielding the average intensity of heatwaves and also can be calculated as the ratio of HWCI to HWF. At the global scale, we use the differences (Δ) between CHW and DHW/NHW to assess the relative changes of CHW over past decades.

2.3. Lagged correlation analysis

Given the time lag between local temperatures and atmospheric circulation anomalies represented by major climate modes (Martens et al., 2018), as well as the varying associations between heatwaves and climate modes across different climate zones, we implemented a two-step approach for our analysis. First, we divided the global map into ten major zones using the Köppen climate classification system (Fig. A9) to account for regional differences. Second, within each climatic zone, we conducted a dynamic correlation analysis to investigate the interannual variability in heatwave events (measured by frequency, intensity, and cumulative intensity) and their relationship with the selected climate mode (Table A1). To calculate the interannual variability of monthly values for each climate variability index, we selected a period commencing one year prior to the heatwave year. To account for potential seasonality, we employed a 3-mon moving window to average the different climate indices. This approach resulted in the generation of 22 monthly interannual series for each climate index, spanning from JFM (January–February–March) of the year before the heatwave to OND (October–November–December) of the current heatwave year. Following this, we performed a lagged correlation analysis between each climate index and the interannual variability of the heatwave, following Eq. (3):

$$r_{\text{lag},i} = \frac{\text{cov}(S, V_i)}{\sigma_S \cdot \sigma_{V_i}} \quad (3)$$

where, the V_i is the climate variability index lagged in the i th month prior to the heatwave event; S indicated the statistical metrics for heatwaves, such as HWI, HWF, and HWCI; $r_{\text{lag},i}$ denotes the corresponding lagged correlation coefficient.

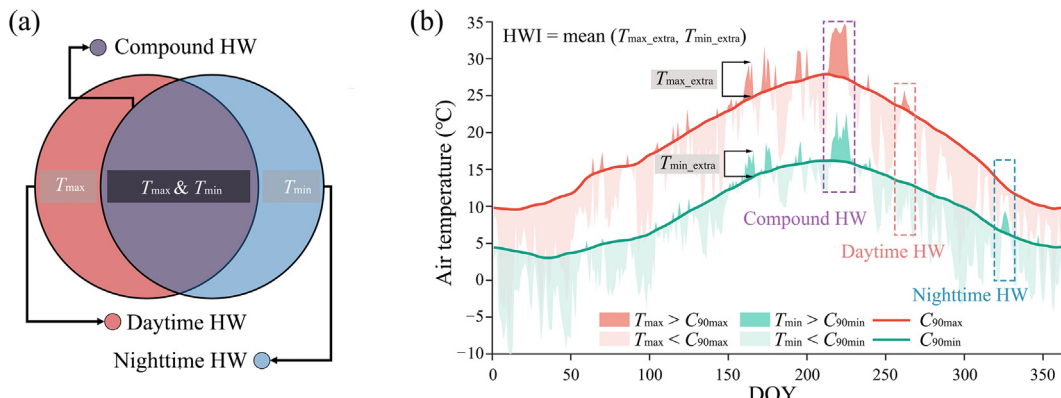


Fig. 1. Conception of different types of heatwaves, (a) schematic diagram of the relationship between CHW, DHW, and NHW, and (b) a case from the grid at 45.88°N, 2.88°E in 2003, demonstrating the difference among CHW, DHW, and NHW within a single year.

3. Results

3.1. Increasing predominance of CHW in recent decades

Our results reveal that on average CHW has consistently exhibited higher values and larger magnitudes of variation across all three metrics over 1980–2022 compared to DHW and NHW. Specifically, CHW demonstrates a higher median frequency of 3.25 d per year and a larger spread ranging from 1.88 to 8.01 d per year, compared to 2.11 d per year (median) and 1.08–1.99 d per year (range) for DHW and 1.57 d per year (median) and 0.75–2.99 d per year (range) for NHW (Fig. 2a). The discrepancy is even more pronounced for HWI, where CHW's median value of 1.56 °C per year is 2.3 times higher than DHW (0.67 °C per year) and 3.3 times higher than NHW (0.47 °C per year) (Fig. 2b). HWCI, which provides a more comprehensive representation of the cumulative impact of heatwaves throughout the year, also exhibits notable differences among the three heatwave types. CHW has a median HWCI of 9.51 °C per year, ranging from 5.13 °C per year to 19.56 °C per year over 1980–2022 (Fig. 2c). In contrast, DHW and NHW display substantially lower HWCI, with their respective maximum values of 4.80 °C per year and 3.95 °C per year, both falling below the minimum value observed for CHW. The spatial distribution of HWCI displays distinct variations among CHW, DHW and NHW, with CHW generally encompassing broader geographical fractions and accounting for over 50% of all types of heatwaves at a global scale (Fig. A1). Overall, these findings highlight the global prevalence of CHW over DHW and NHW, emphasizing the need for increased attention on CHW events.

To further investigate the decadal trends of CHW compared to DHW/NHW, we assessed the temporal change rates of annual HWF, HWI, and HWCI individually, as well as the anomaly trends of the difference (Δ) between CHW and DHW/NHW (Fig. 3). Focusing on frequency (HWF), the linear regression slope of CHW reaches 1.60 d per decade over the past 43 years on a global scale, nearly tripling the linear

trend of DHW (0.59 d per decade) (Fig. 3a). Notably, the linear trend for NHW frequencies has increased to 1.06 d per decade, indicating a significant rise in NHW occurrences. Concurrently, Δ HWF exhibits a linear upward trend of 1.01 and 0.54 d per decade for CHW relative to DHW and NHW, respectively (Fig. 3b). This growing trend in Δ HWF has impacted almost 70% of Earth's land (Fig. 3a and b), with the most widespread increases in Δ HWF contributed by the drylands and continental climate zone in the Northern Hemisphere (Fig. A2a–b). However, significant declines ($p < 0.001$) in Δ HWF (CHW vs. NHW) are predominantly found in Southeast Asia and the western tropical Africa, contributing up to ~40% to the overall global increase in Δ HWF (Fig. A2b).

Regarding intensity (HWI), the trend of CHW shows a significant increase of 0.16 °C per decade, surpassing the corresponding trends of DHW and NHW (0.06 °C per decade) (Fig. 3c). Meanwhile, their Δ HWIs exhibit a similar increasing trend, with values of 0.10 and 0.09 °C per decade, respectively (Fig. 3d). While the ratio of the increasing area for Δ HWI is slightly higher than that of Δ HWF, the spatial pattern differs notably, with the most pronounced increments in Δ HWI primarily concentrated in the Northern Hemisphere, particularly in Eurasia (Fig. 4c and d). Among these, the dryland and continental regions in the Northern Hemisphere contribute about 50% of the global increase in Δ HWI (Fig. A2c–d). Such spatial differences can be mainly attributed to the influence of synoptic systems and surface conditions in arid and high-latitude regions (including continental and polar climates). For instance, subtropical high-pressure systems are associated with more stable atmospheric structures. Atmospheric subsidence within these systems suppresses the vertical movement of heat, hindering the dissipation of heat near the surface and thereby maintaining elevated nighttime temperatures. Furthermore, decreased surface albedo results in greater absorption of solar radiation by the surface, and the stored heat is released continuously during the night, prolonging periods of high temperatures. In examining HWCI, which serves as an

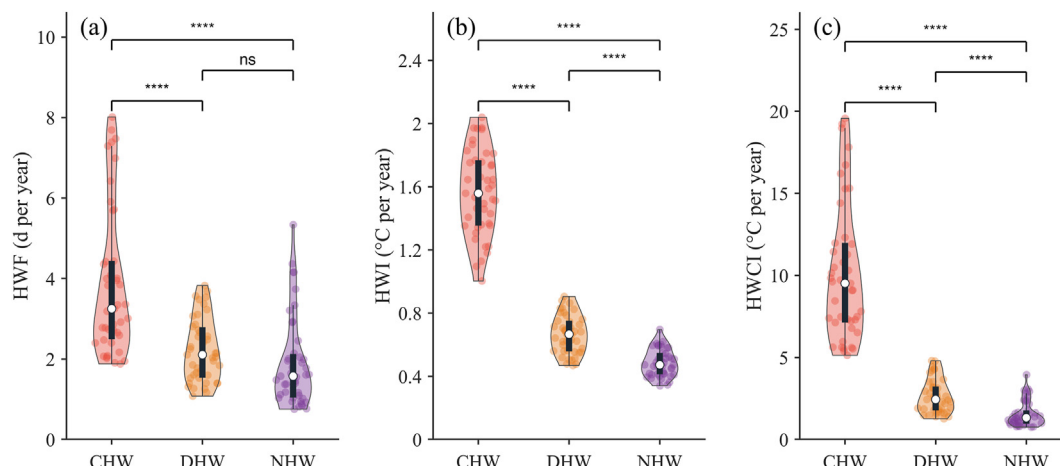


Fig. 2. Comparison of annual (a) frequency (HWF), (b) intensity (HWI), and (c) cumulative intensity (HWCI) among global CHW, DHW, and NHW from 1980 to 2022 (Statistical significance was tested using the t -test, where asterisks (****) denote $p < 0.0001$, and ns indicates a non-significant difference with $p > 0.05$).

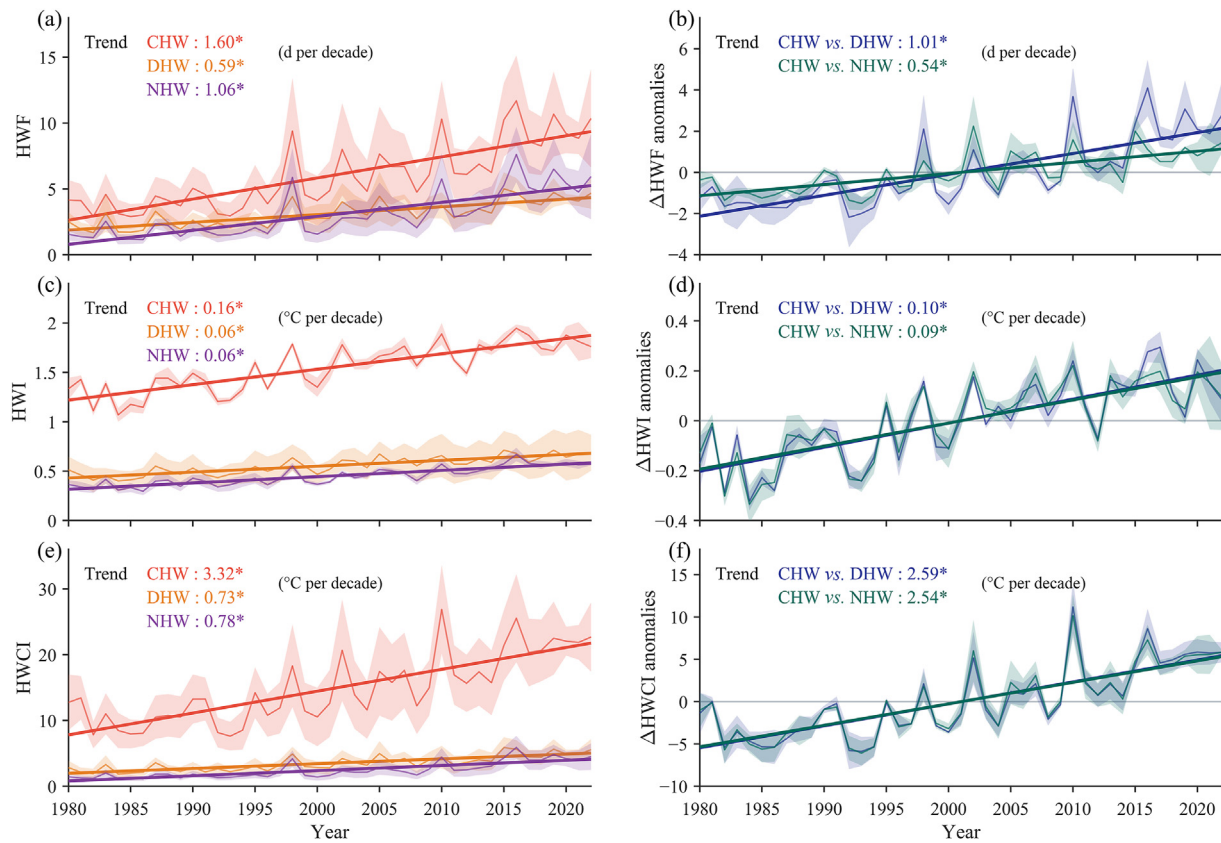


Fig. 3. Time series of global CHW, DHW, and NHW from 1980 to 2022, (a) annual frequency (HWF), (c) annual intensity (HWI), and (e) annual cumulative intensity (HWCI); the annual anomalies of differences (Δ) between CHW and DHW/NHW in the metrics of (b) Δ HWF, (d) Δ HWI, and (f) Δ HWCI (The shaded area indicates the above metrics obtained from two independent reanalysis products (*i.e.*, MERRA2 and JRA55). The asterisks (*) denote that the trend passed the Mann–Kendall test ($p < 0.001$)).

integrated measure of both HWF and HWI, CHW exhibits a notable linear increasing trend, with a magnitude of 3.32°C per decade, surpassing the trends of DHW (0.73°C per decade) and NHW (0.78°C per decade) by a factor of four (Fig. 3e). The trend of Δ HWCI in relation to DHW and NHW exhibits similar values of 2.59 and 2.54°C per decade, respectively (Fig. 3f). These results collectively demonstrate the increasing predominance of CHW over DHW and NHW in recent decades in terms of frequency, intensity, and cumulative intensity.

3.2. Global trend and temporal evolution of CHW

Given that CHW exhibits substantially higher mean annual frequency and intensity, as well as 2–4 times greater increasing trends compared to DHW and NHW, next we primarily focus on global trend and temporal evolution of CHW. Over the past 43 years, there has been a general increase in annual HWF, HWI, and HWCI at a global scale (Fig. 5). The Arctic Circle and certain tropical regions (*e.g.*, Amazon basin and upper Nile) have experienced the most pronounced increase in HWF, with a zonal mean value of increasing rates exceeding 0.3 d per year (Fig. 5a). The Arctic, in particular,

has encountered more frequent heatwaves, typically surpassing 10 days annually, especially after 2005 (Fig. 5b).

In comparison, the increasing trend of HWI is more geographically widespread (especially in Eurasia) than that of HWF (Fig. 5c). Temporal variations in latitudinal profile reveal that the increase in HWI has expanded from high to low latitudes since 1980, with the most significant increase occurring north of 45°N since 2000 (Fig. 5d). Furthermore, the annual HWCI, an indicator of integrated heat stress, has exhibited a significant increase from 1980 to 2022 (Fig. 5e). The high latitudes of the Northern Hemisphere have experienced an annual growth rate exceeding 1.2°C per year, which is notably higher than the growth rate in other global regions and highly consistent with the effect areas of Arctic amplification (Ono et al., 2022; Serreze and Francis, 2006). This trend has become more pronounced after 2000, as illustrated by the time evolution of the latitudinal mean profile (Fig. 5f).

We further explored temporal trends and mean annual values of HWF, HWI, and HWCI for each grid cell in the climatological space (Fig. 6). Our results indicate that almost all climatological spaces exhibit increasing CHW trends, regardless of the specific metric being analyzed. Nonetheless, the most pronounced rise in the trend of HWF appears in

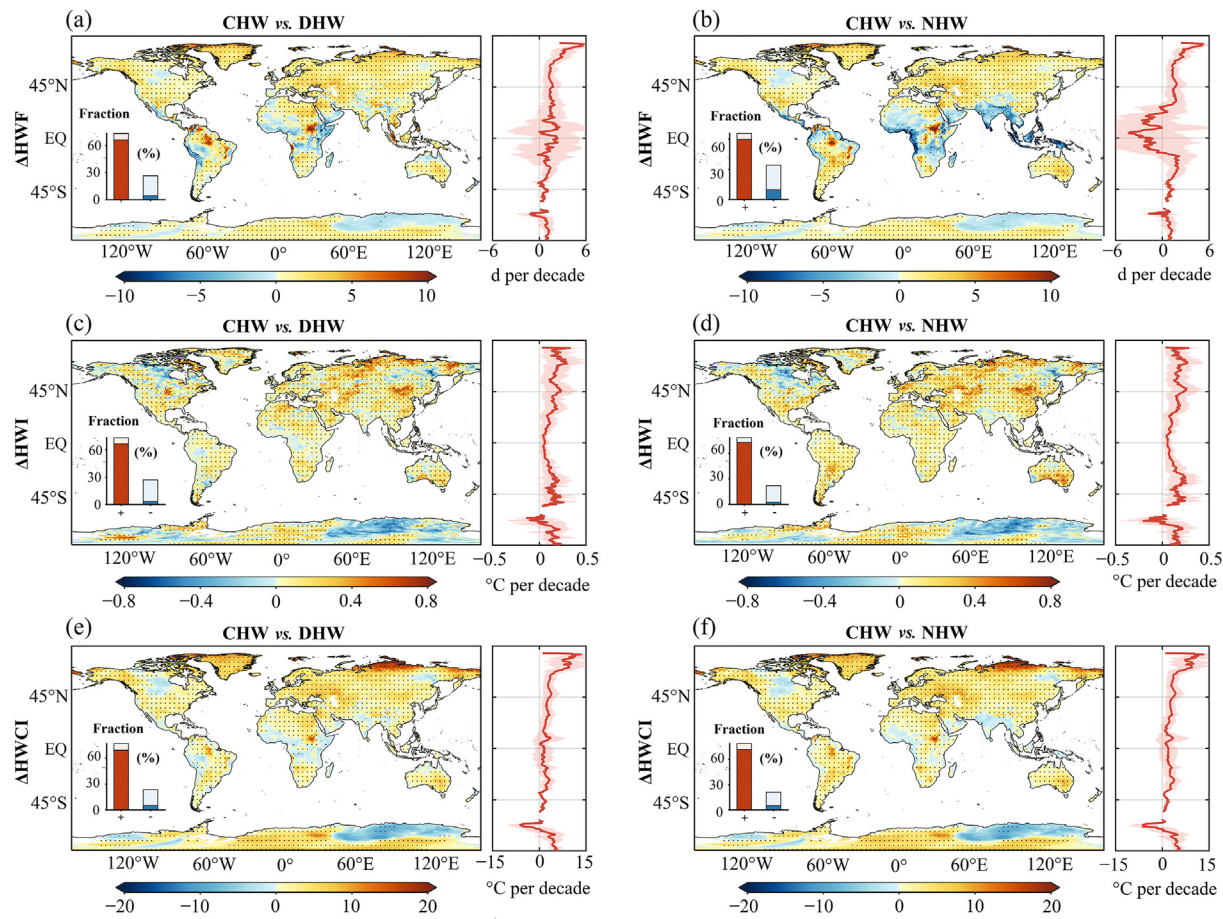


Fig. 4. Global trend maps of ΔHWF , ΔHWI , and ΔHWCI from 1980 to 2022, comparing CHW vs. DHW (a, c, e) and CHW vs. NHW (b, d, f) (Bar-plot in each sub-panel indicate the increasing (+)/decreasing (-) area fraction to the total land surface. Light colors in bar-plot denote the overall fraction, while dark colors denote the significant fraction ($p < 0.001$). The right panel in each sub-plot displays the zonally averaged profiles based on the trend map, considering only significant grid cells for the calculation).

regions with a mean annual air temperature (MAAT) exceeding 20 °C and mean annual precipitation (MAP) over 1000 mm, as well as in regions with MAAT ranging between -10 and 0 °C and MAP exceeding 1500 mm (Fig. 6a). Mean annual HWF analysis shows a similar pattern to HWF trend, with cold (MAAT < 0 °C) and humid (MAP > 1500 mm) regions are more susceptible to CHW (Fig. 6d). The difference between trend and mean annual pattern is most evident for HWI (Fig. 6b–e), with the highest increasing trend in regions with a MAAT of approximately 5 °C, while remaining stable in hot-humid or cold-arid regions in recent decades (Fig. 6b). Conversely, the mean annual HWCI exhibits substantially higher values in cold regions, particularly with MAAT < -5 °C (Fig. 6f). For HWCI trend, there exist two hotspots with the most notable increase: cold-humid regions (MAP > 1000 mm) and cold-arid regions (MAP < 500 mm) with a MAAT between -25 and -5 °C (Fig. 6c).

Collectively, these findings suggest that cold regions are more susceptible to CHW, with the increasing trend expanding into warmer, lower-latitude regions (Figs. 5 and 6). Our analysis of both temporal trend and mean annual values highlights the importance of continued monitoring and

adaptive measures at mid-to-high latitudes in order to address the evolving consequences of compound heatwaves.

3.3. Connections between climate modes and interannual CHW variability

To further elucidate the underlying factors driving the interannual trends in CHW, we investigate the potential connections between CHW variability and climate modes, which are responsible for anomalies in large-scale atmospheric circulation. The global terrestrial area is divided into ten climate zones based on the Köppen climate classification (Fig. A9), separately for the Northern and Southern Hemisphere. We then assessed the time-series relationships between CHW and major climate modes within each climate zone, primarily focusing on HWCI (Fig. 7), while observing similar patterns for HWF and HWI (Fig. A3 and Fig. A4).

Our results reveal that HWCI exhibits strong associations with various climate modes across different climate zones and hemispheres (Fig. 7). In the tropics, HWCI is highly correlated with the El Niño–Southern Oscillation (ENSO) and the Pacific Decadal Oscillation (PDO) in both hemispheres. Indeed, the

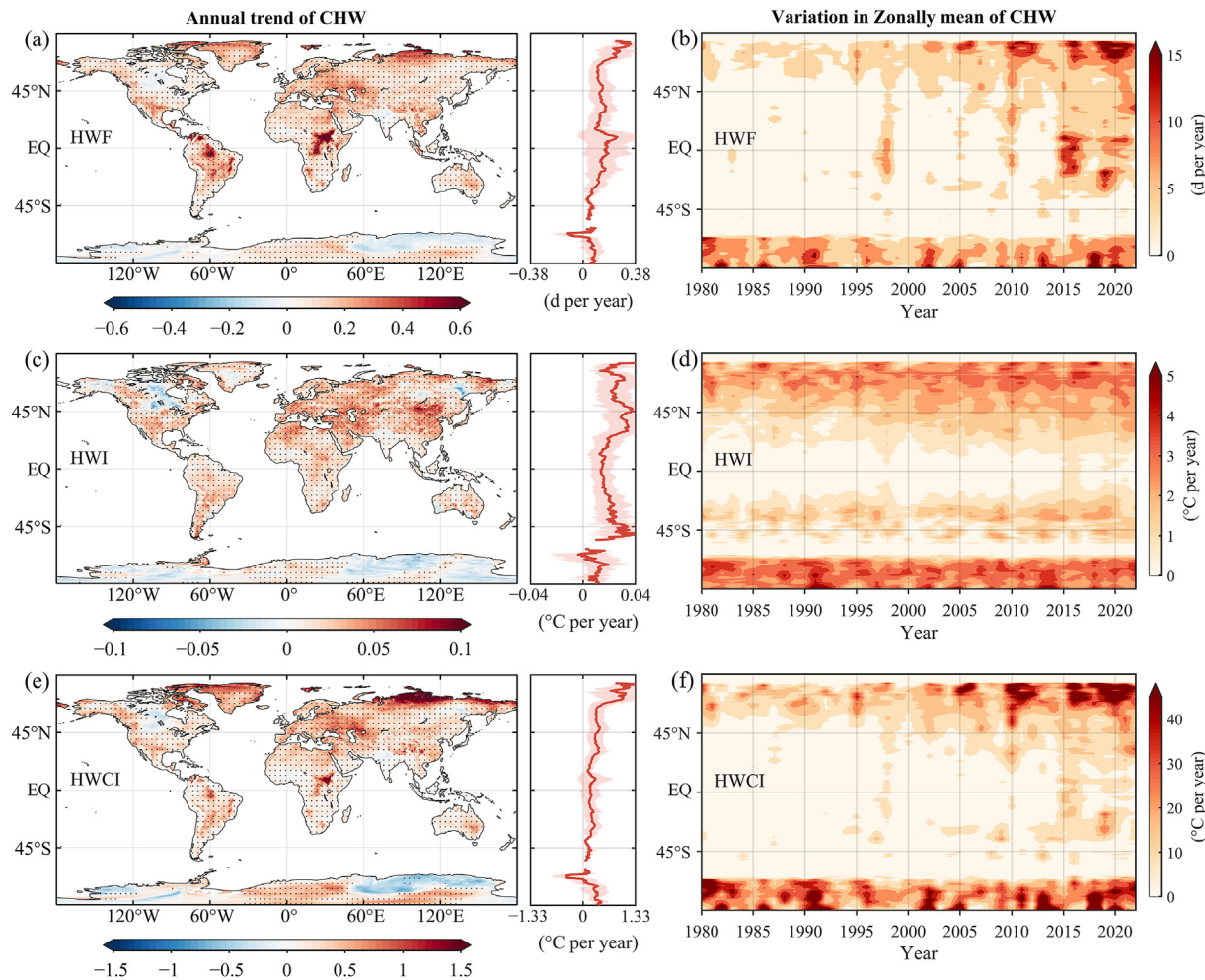


Fig. 5. The grid-based annual trends of CHW in terms of (a) frequency (HWF), (c) intensity (HWI), and (e) cumulative intensity (HWCI), accompanied by their zonally averaged profiles (b, d, f) in latitudinal distribution, during 1980–2022 (Black dots in map indicate the grid cells with significant trend ($p < 0.001$)).

tropics undergo more severe CHW during El Niño years (e.g., 1998, 2010, and 2015), compared to normal years (Fig. A5–A7). Moreover, ENSO and PDO display significant lag effects on CHW that begins in June of the year preceding the heatwave year and lasts for approximately one year, which coincides with the typical life cycle of ENSO events. Our findings, therefore, suggest the dominant role of ENSO in shaping the interannual variability of CHW events within the tropics.

In drylands and temperate climate zones, ENSO and PDO remain main drivers of HWCI, albeit with weakened relationships and shorter lag durations compared to the tropics. Their associations also differ between hemispheres, particularly for PDO, which only strongly associates with HWCI in the Southern Hemisphere. Such discrepancy between hemispheres stems from PDO displaying high correlations with HWF in both hemispheres (Fig. A3) but inconsistent correlations with HWI between hemispheres (Fig. A4). Additionally, the Eastern Pacific North Pacific (EPNP) mode exhibits relatively strong correlations with HWCI in the Southern Hemisphere, and similar to ENSO and PDO, its correlation period is shorter in these regions.

The associations between CHW and climate modes generally weaken in the continental climate zone, except for the East Atlantic/West Russia (EAWR) pattern, which demonstrates a relatively high correlation with CHW in the Northern Hemisphere for a short duration. In polar regions, dominant climate modes vary substantially between hemispheres. The Arctic exhibits stronger CHW linkages with EAWR and the Atlantic Multidecadal Oscillation (AMO) for a short duration, but both relationships are at the moderate level. In contrast, CHW in Antarctica demonstrates a significant negative correlation with the Southern Annular Mode (SAM) and the Antarctic Oscillation (AAO) from March to September in the heatwave year. The occurrence of blocking days in Antarctica is found to closely relate to the AAO (Marín et al., 2022), and both SAM and AAO importantly regulate Antarctic temperature fluctuations (Mayewski et al., 2009).

4. Discussion

This study reveals a significant intensification of CHW on a global scale when compared to DHW and NHW counterparts. This finding is consistent across the three heatwave metrics

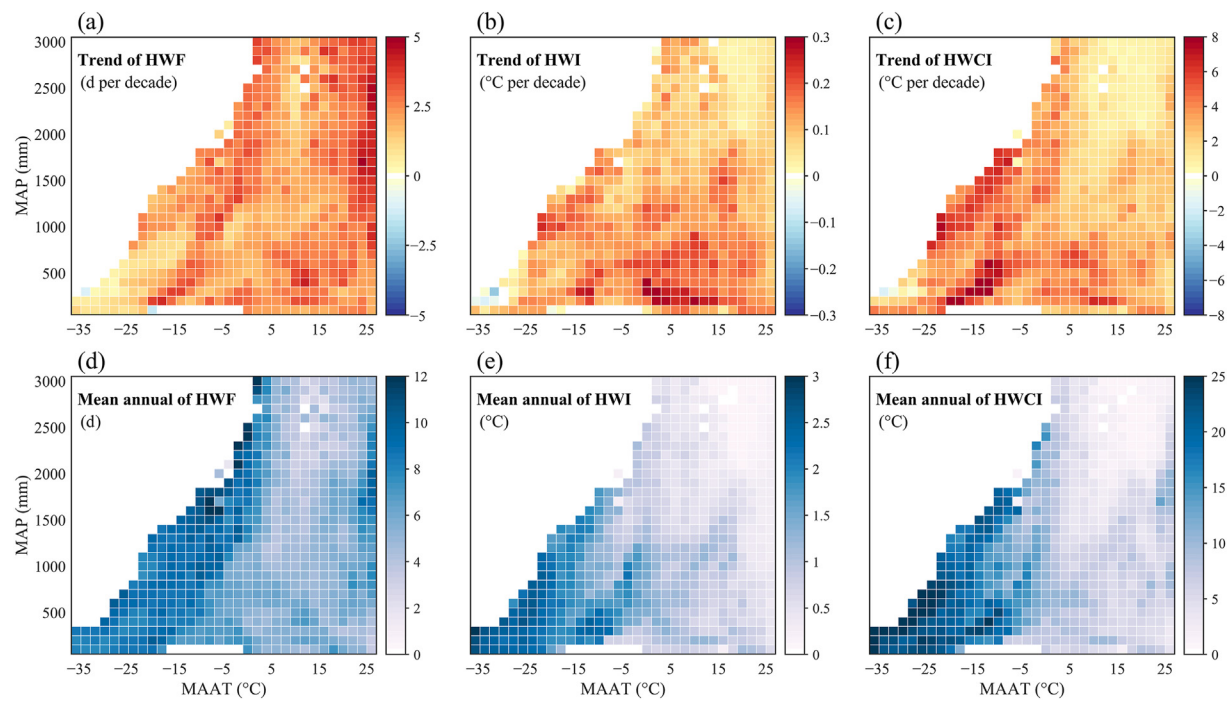


Fig. 6. Spatial distribution of global trends (a, b, c) and mean annual values (d, e, f) for HWF, HWI, and HWCI from 1980 to 2022 (The space is categorized by climatological temperature (MAAT) and precipitation (MAP)).

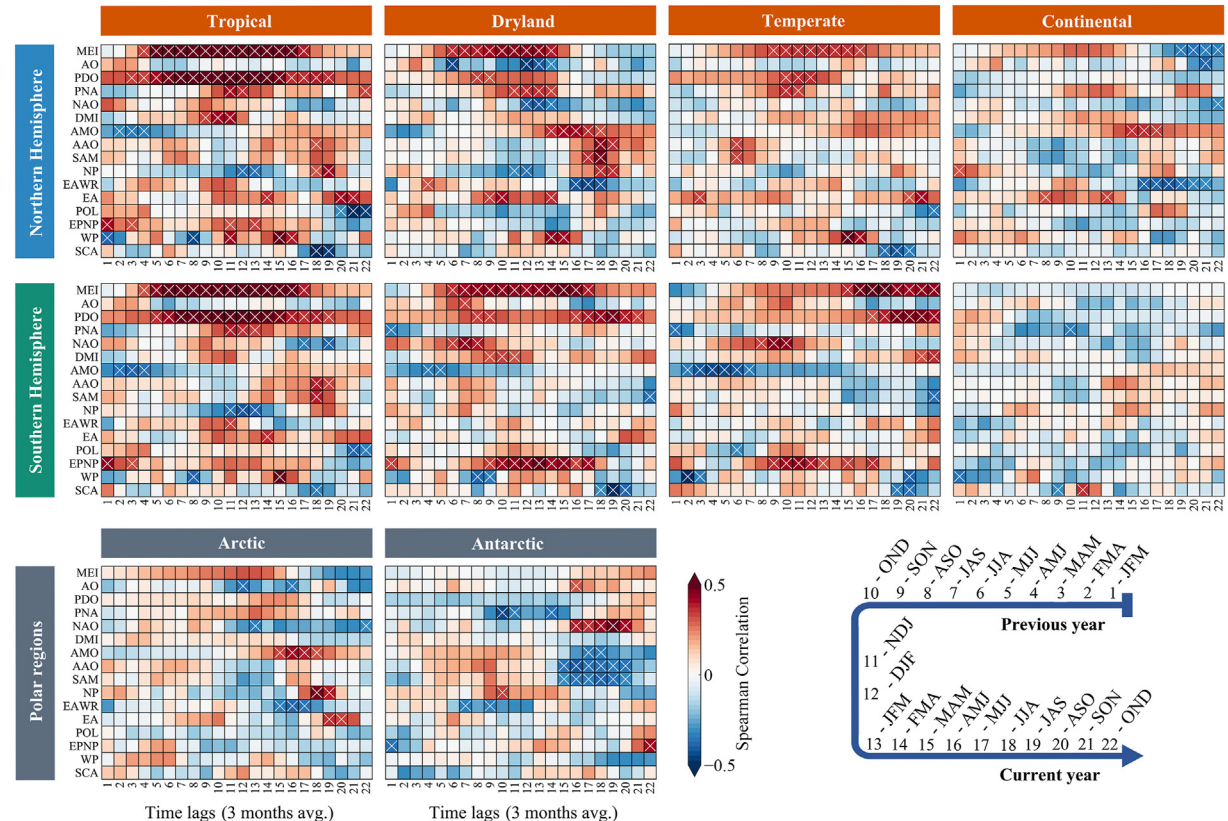


Fig. 7. Lagged correlation between HWCI of CHW and 16 modes of climate variability across different climate zones. (The x-axis represents the time dynamics of different monthly climate indices correlated to HWCI, considering both the current year and the previous year, with the climate index calculated as a 3-mon average. White crosses indicate that the correlation passed the significance test ($p < 0.05$).

examined, as well as in temporal (Fig. 3) and spatial (Fig. 4) analyses. Moreover, we found that the frequency of NHW has increased at a rate of 1.06 d per decade, which is twice the growth rate of DHW (Fig. 3a), while the rate of NHW intensity is similar to that of DHW (Fig. 3c). These findings suggest that while nighttime high-temperature extremes have become markedly more frequent globally, their intensity is not significantly greater compared to daytime hot extremes. Notably, compared to individual-type heatwaves, CHW have experienced a remarkably higher growth rate. For instance, as indicated in HWCI, the growth rate of CHW is 3.32 °C per decade (Fig. 3e), more than four times greater than that of DHW/NHW. This relatively stronger growth rate has become particularly pronounced since 2000, highlighting the increasing prevalence of global CHW. The cause of extremely hot conditions in both daytime and nighttime can be attributed to the enhanced water vapor associated with the background rising air temperature (Miralles et al., 2014). This process contributes to increased atmospheric moisture, which in turn traps more heat at the Earth's surface during the daytime and subsequently raises the likelihood of extreme nighttime heat (Byrne and O'Gorman, 2018; Chemke et al., 2016). Consequently, in the context of global warming and heightened humidity, CHW events characterized by both daytime and nighttime hot conditions have become increasingly prevalent across both space and time, subjecting natural ecosystems and human well-beings to intensified heat stress.

Furthermore, our findings reveal substantial spatiotemporal heterogeneity in the annual trends of global CHW, with the most pronounced changes observed in high-latitude and cold regions, particularly in the polar regions (Figs. 4–6). This spatial pattern is corroborated by recent observations of record-breaking Arctic heatwaves (Dobricic et al., 2020; Simpkins, 2017). Lower historical temperature thresholds (Fig. A8) and increased solar radiation absorption due to reduced albedo from melting ice and snow make cold regions like the Arctic more sensitive to extreme hot events (Francis et al., 2017). Moreover, the lack of vegetation in these regions contributes to greater temperature variability and diminished capacity for thermal regulation (Guo et al., 2023; O et al., 2022). This biophysical limitation results from reduced evapotranspiration and lower heat storage in unvegetated surfaces, exacerbating the magnitude of temperature fluctuations during hot extremes. The instability of the polar vortex also contributes to greater temperature fluctuations in polar regions compared to other locations (Zhang et al., 2016). The combined factors render polar and high-latitude regions particularly vulnerable to climate change and severely affected by CHW. However, Antarctic heatwaves do not show a significant increase on a temporal scale and even a decrease in the northeastern part (Fig. 5). This is likely caused by the insignificant Antarctic warming, which is due to its relatively independent climate system and the potentially mitigating effect of the ozone hole that slows down the warming trend in this area (Hartmann, 2022; Thompson et al., 2011).

Changes in global climate patterns are intricately connected among different Earth system components, with complex

underlying mechanisms that can be partly characterized by their connections with major climate modes (Hernández et al., 2020). Our study reveals that tropics undergo more severe CHW during El Niño years, such as 1998, 2010, and 2015, as compared to normal years (Fig. A5–A7). This observation is further supported by significant correlations of CHW with ENSO and PDO, and correlation pattern exhibits noticeable lag effects, initiating in June of the year preceding heatwave occurrences (Fig. 7, Figs. A3–A4). Such association between CHW and ENSO/PDO can be attributed to the weakening of the Walker Circulation during El Niño episodes. This weakening results in a replacement of rising air with an anomalous sinking branch over the Amazon and Southeast Asia (Power and Smith, 2007), leading to reduced rainfall in these regions (Asner et al., 2000; Luther et al., 1983). In addition, the weakened trade winds along the equator obstruct the exchange of advection flow, thereby increasing the likelihood of blocking synoptic systems that promote heat accumulation (Kang et al., 2018; Kautz et al., 2022).

In addition, we also found that internal climate variability modes exhibit weaker associations with interannual CHW variations in extratropical regions compared to tropics (Fig. 7). These weakened relationships and shorter significant correlation durations imply that processes beyond climate mode effects, such as land–atmosphere coupling, also play crucial roles in regulating widespread heatwave evolution and propagation in these areas. While this study highlights the role of climate variability modes, we acknowledge that land–atmosphere feedbacks remain insufficiently explored to fully characterize their contributions to global CHW dynamics. The land–atmosphere feedback is usually more pronounced in drylands (water-limited region) and temperate (transitional region) climate zones (Orth et al., 2020; Seneviratne et al., 2010), which modulates extreme hot temperatures by distributing available surface energy into sensible heating through the regulation of soil moisture and evapotranspiration (Schumacher et al., 2020; Vogel et al., 2017). In continental zones (primarily boreal areas) and Arctic regions, such land feedbacks manifest as Arctic Amplification (Ono et al., 2022; Serreze and Francis, 2006), which operates by producing positive feedbacks on accelerated sea ice and snow cover melting (Cohen et al., 2014). This mechanism is increasingly recognized as a major driver of accelerated warming in mid-to-high latitudes of the Northern Hemisphere. Future quantification of land feedbacks on temperature amplification will be critical for advancing our understanding of CHW variability under climate change.

5. Conclusions

Our finding reveals a four times greater predominance of CHW driving global heatwaves over 1980–2022 in all metrics. The growing prominence of elevated nighttime temperatures coincides with the increasing predominance of CHW in recent decades. Mid-to-high-latitudes in the Northern Hemisphere are more susceptible to CHW. These regions exhibit relatively weak associations with modes of climate variability,

tend to be more influenced by local land–atmosphere feedback and Arctic amplification. However, the spatial variation and temporal trends of CHW are tightly connected to climate variability in tropics, such as ENSO and PDO. The prevalence of CHW has crucial and timely real-world implications for ecosystems and human society due to their more destructive effects. The significant connections between CHWs and specific climate modes allow us for proactive measures based on correlation duration. Moreover, modulating local water and energy exchanges can potentially mitigate temperature amplification in water limited regions, and reducing greenhouse gas emissions and achieving carbon neutrality is essential to lessen harmful effects and occurrences of CHW.

Declaration of competing interest

The authors declare no conflict of interest.

CRediT authorship contribution statement

Kun Zhang: Writing – review & editing, Writing – original draft, Methodology, Conceptualization. **Jin-Bao Li:** Writing – review & editing, Conceptualization. **Michael Kwok-Po Ng:** Writing – review & editing, Supervision. **Zheng-Fei Guo:** Formal analysis. **Amos P.K. Tai:** Writing – review & editing. **Shu-Wen Liu:** Investigation. **Xiao-Rong Wang:** Writing – review & editing. **Jie Zhang:** Writing – review & editing. **Jin Wu:** Writing – review & editing, Funding acquisition, Conceptualization.

Acknowledgments

The work was primarily supported by National Natural Science Foundation of China (31922090), National Key Research and Development Program of China (2018YFA0605601), Hong Kong Research Grant Council General Research Fund (17316622 and 17305321). Jin Wu was also supported by the HKU Seed Funding for Strategic Interdisciplinary Research Scheme, the Hung Ying Physical Science Research Fund (2021–22), and the Innovation and Technology Fund (funding support to State Key Laboratory of Agrobiotechnology).

Appendix A. Supplementary data

Supplementary data to this article can be found online at <https://doi.org/10.1016/j.accre.2025.04.010>.

References

- Alexander, M.A., Bladé, I., Newman, M., et al., 2002. The atmospheric bridge: the influence of ENSO teleconnections on air–sea interaction over the global oceans. *J. Clim.* 15, 2205–2231. [https://doi.org/10.1175/1520-0442\(2002\)015<2205:TABTI>2.0.CO;2](https://doi.org/10.1175/1520-0442(2002)015<2205:TABTI>2.0.CO;2).
- Anderegg, W.R.L., Kane, J.M., Anderegg, L.D.L., 2013. Consequences of widespread tree mortality triggered by drought and temperature stress. *Nat. Clim. Change* 3, 30–36. <https://doi.org/10.1038/nclimate1635>.
- Asner, G.P., Townsend, A.R., Braswell, B.H., 2000. Satellite observation of El Niño effects on Amazon forest phenology and productivity. *Geophys. Res. Lett.* 27, 981–984. <https://doi.org/10.1029/1999GL011113>.
- Baldwin, J.W., Dessy, J.B., Vecchi, G.A., et al., 2019. Temporally compound heat wave events and global warming: an emerging hazard. *Earth's Future* 7, 411–427. <https://doi.org/10.1029/2018EF000989>.
- Brás, T.A., Seixas, J., Carvalhais, N., et al., 2021. Severity of drought and heatwave crop losses tripled over the last five decades in Europe. *Environ. Res. Lett.* 16, 065012. <https://doi.org/10.1088/1748-9326/abf004>.
- Byrne, M.P., O'Gorman, P.A., 2018. Trends in continental temperature and humidity directly linked to ocean warming. *Proc. Natl. Acad. Sci.* 115, 4863–4868. <https://doi.org/10.1073/pnas.1722312115>.
- Chemke, R., Kaspi, Y., Halevy, I., 2016. The thermodynamic effect of atmospheric mass on early Earth's temperature. *Geophys. Res. Lett.* 43 (11), 414. <https://doi.org/10.1002/2016GL071279>, 11,422.
- Chen, Y., Zhai, P., 2017. Revisiting summertime hot extremes in China during 1961–2015: overlooked compound extremes and significant changes. *Geophys. Res. Lett.* 44, 5096–5103. <https://doi.org/10.1002/2016GL072281>.
- Ciais, P., Reichstein, M., Viovy, N., et al., 2005. Europe-wide reduction in primary productivity caused by the heat and drought in 2003. *Nature* 437, 529–533. <https://doi.org/10.1038/nature03972>.
- Cohen, J., Screen, J.A., Furtado, J.C., et al., 2014. Recent Arctic amplification and extreme mid-latitude weather. *Nat. Geosci.* 7, 627–637. <https://doi.org/10.1038/ngeo2234>.
- Dobricic, S., Russo, S., Pozzoli, L., et al., 2020. Increasing occurrence of heat waves in the terrestrial Arctic. *Environ. Res. Lett.* 15, 024022. <https://doi.org/10.1088/1748-9326/ab6398>.
- Fischer, E.M., Schär, C., 2010. Consistent geographical patterns of changes in high-impact European heatwaves. *Nat. Geosci.* 3, 398–403. <https://doi.org/10.1038/ngeo866>.
- Fischer, E.M., Sippel, S., Knutti, R., 2021. Increasing probability of record-shattering climate extremes. *Nat. Clim. Change* 11, 689–695. <https://doi.org/10.1038/s41558-021-01092-9>.
- Francis, J.A., Vavrus, S.J., Cohen, J., 2017. Amplified Arctic warming and mid-latitude weather: new perspectives on emerging connections. *Wires Clim. Change* 8, e474. <https://doi.org/10.1002/wcc.474>.
- Gelaro, R., McCarty, W., Suárez, M.J., et al., 2017. The modern-era retrospective analysis for research and applications, version 2 (MERRA-2). *J. Clim.* 30, 5419–5454. <https://doi.org/10.1175/JCLI-D-16-0758.1>.
- Guo, Z., Still, C.J., Lee, C.K.F., et al., 2023. Does plant ecosystem thermoregulation occur? An extratropical assessment at different spatial and temporal scales. *New Phytol.* 238, 1004–1018. <https://doi.org/10.1111/nph.18632>.
- Hartmann, D.L., 2022. The Antarctic ozone hole and the pattern effect on climate sensitivity. *Proc. Natl. Acad. Sci.* 119, e2207889119. <https://doi.org/10.1073/pnas.2207889119>.
- Hernández, A., Martín-Puertas, C., Moffa-Sánchez, P., et al., 2020. Modes of climate variability: synthesis and review of proxy-based reconstructions through the Holocene. *Earth Sci. Rev.* 209, 103286. <https://doi.org/10.1016/j.earscirev.2020.103286>.
- Hersbach, H., Bell, B., Berrisford, P., et al., 2020. The ERA5 global reanalysis. *Q. J. R. Meteorol. Soc.* 146, 1999–2049. <https://doi.org/10.1002/qj.3803>.
- Kang, S.M., Shin, Y., Xie, S.-P., 2018. Extratropical forcing and tropical rainfall distribution: energetics framework and ocean Ekman advection. *npj Climate and Atmospheric Science* 1, 1–10. <https://doi.org/10.1038/s41612-017-0004-6>.
- Kautz, L.-A., Martius, O., Pfahl, S., et al., 2022. Atmospheric blocking and weather extremes over the Euro-Atlantic sector: a review. *Weather and Climate Dynamics* 3, 305–336. <https://doi.org/10.5194/wcd-3-305-2022>.
- Kobayashi, S., Ota, Y., Harada, Y., et al., 2015. The JRA-55 reanalysis: general specifications and basic characteristics. *Meteorol. Soc. Japan. Ser. II* 93, 5–48. <https://doi.org/10.2151/jmsj.2015-001>.
- Li, J., Tam, C.-Y., Tai, A.P.K., et al., 2021. Vegetation–heatwave correlations and contrasting energy exchange responses of different vegetation types to summer heatwaves in the Northern Hemisphere during the 1982–2011 period. *Agric. For. Meteorol.* 296, 108208. <https://doi.org/10.1016/j.agrformet.2020.108208>.

- Liang, C.-M., Zhao, L., Zhou, S.-W., et al., 2023. Rapid increase in warm-wet compound extreme events with high health risks in southern China: joint influence of ENSO and the Indian ocean. *Adv. Clim. Change Res.* 14, 856–865. <https://doi.org/10.1016/j.accre.2023.11.008>.
- Liao, Z., Yuan, Y.-F., Chen, Y., et al., 2024. Extraordinary hot extreme in summer 2022 over the yangtze river basin modulated by the la niña condition under global warming. *Adv. Clim. Change Res.* 15, 21–30. <https://doi.org/10.1016/j.accre.2023.12.006>.
- Luo, M., Lau, N.-C., 2021. Increasing human-perceived heat stress risks exacerbated by urbanization in China: a comparative study based on multiple metrics. *Earths Future* 9, e2020EF001848. <https://doi.org/10.1029/2020EF001848>.
- Luo, M., Lau, N.-C., 2020. Summer heat extremes in northern continents linked to developing ENSO events. *Environ. Res. Lett.* 15, 074042. <https://doi.org/10.1088/1748-9326/ab7d07>.
- Luo, M., Lau, N.-C., Liu, Z., 2022. Different mechanisms for daytime, nighttime, and compound heatwaves in southern China. *Weather Clim. Extrem.* 36, 100449. <https://doi.org/10.1016/j.wace.2022.100449>.
- Luther, D.S., Harrison, D.E., Knox, R.A., 1983. Zonal winds in the central equatorial pacific and El Niño. *Science* 222, 327–330. <https://doi.org/10.1126/science.222.4621.327>.
- Ma, F., Yuan, X., Wu, P., et al., 2022. A moderate mitigation can significantly delay the emergence of compound hot extremes. *J. Geophys. Res. Atmos.* 127, e2021JD035427. <https://doi.org/10.1029/2021JD035427>.
- Ma, K., Gong, H., Wang, L., et al., 2024. Anthropogenic forcing intensified internally driven concurrent heatwaves in August 2022 across the Northern Hemisphere. *NPJ Clim. Atmos. Sci.* 7, 1–9. <https://doi.org/10.1038/s41612-024-00828-6>.
- Marín, J.C., Bozkurt, D., Barrett, B.S., 2022. Atmospheric blocking trends and seasonality around the Antarctic peninsula. *J. Clim.* 35, 3803–3818. <https://doi.org/10.1175/JCLI-D-21-0323.1>.
- Martens, B., Waegeman, W., Dorigo, W.A., et al., 2018. Terrestrial evaporation response to modes of climate variability. *NPJ Clim. and Atmos. Sci.* 1, 43. <https://doi.org/10.1038/s41612-018-0053-5>.
- Mayewski, P.A., Meredith, M.P., Summerhayes, C.P., et al., 2009. State of the Antarctic and southern ocean climate system. *Rev. Geophys.* 47. <https://doi.org/10.1029/2007RG000231>.
- Miralles, D.G., van den Berg, M.J., Gash, J.H., et al., 2014. El Niño–La Niña cycle and recent trends in continental evaporation. *Nat. Clim. Change* 4, 122–126. <https://doi.org/10.1038/nclimate2068>.
- O, S., Bastos, A., Reichstein, M., et al., 2022. The role of climate and vegetation in regulating drought–heat extremes. *J. Clim.* 35, 5677–5685. <https://doi.org/10.1175/JCLI-D-21-0675.1>.
- Ono, J., Watanabe, M., Komuro, Y., et al., 2022. Enhanced Arctic warming amplification revealed in a low-emission scenario. *Commun. Earth Environ.* 3, 1–9. <https://doi.org/10.1038/s43247-022-00354-4>.
- Orth, R., Destouni, G., Jung, M., et al., 2020. Large-scale biospheric drought response intensifies linearly with drought duration in arid regions. *Bio-geosciences* 17, 2647–2656. <https://doi.org/10.5194/bg-17-2647-2020>.
- Park Williams, A., Allen, C.D., Macalady, A.K., et al., 2013. Temperature as a potent driver of regional forest drought stress and tree mortality. *Nat. Clim. Change* 3, 292–297. <https://doi.org/10.1038/nclimate1693>.
- Parker, T.J., Berry, G.J., Reeder, M.J., et al., 2014. Modes of climate variability and heat waves in Victoria, southeastern Australia. *Geophys. Res. Lett.* 41, 6926–6934. <https://doi.org/10.1002/2014GL061736>.
- Perkins, S.E., Argüeso, D., White, C.J., 2015. Relationships between climate variability, soil moisture, and Australian heatwaves. *J. Geophys. Res. Atmos.* 120, 8144–8164. <https://doi.org/10.1002/2015JD023592>.
- Perkins-Kirkpatrick, S., Barriopedro, D., Jha, R., et al., 2024. Extreme terrestrial heat in 2023. *Nat. Rev. Earth Environ.* 5, 244–246. <https://doi.org/10.1038/s43017-024-00536-y>.
- Perkins-Kirkpatrick, S.E., Lewis, S.C., 2020. Increasing trends in regional heatwaves. *Nat. Commun.* 11, 3357. <https://doi.org/10.1038/s41467-020-16970-7>.
- Power, S.B., Smith, I.N., 2007. Weakening of the Walker Circulation and apparent dominance of El Niño both reach record levels, but has ENSO really changed? *Geophys. Res. Lett.* 34. <https://doi.org/10.1029/2007GL030854>.
- Reddy, P.J., Perkins-Kirkpatrick, S.E., Ridder, N.N., et al., 2022. Combined role of ENSO and IOD on compound drought and heatwaves in Australia using two CMIP6 large ensembles. *Weather Clim. Extrem.* 37, 100469. <https://doi.org/10.1016/j.wace.2022.100469>.
- Russo, S., Dosio, A., Graversen, R.G., et al., 2014. Magnitude of extreme heat waves in present climate and their projection in a warming world. *J. Geophys. Res. Atmos.* 119 (12). <https://doi.org/10.1002/2014JD022098>, 500–12,512.
- Russo, S., Sillmann, J., Fischer, E.M., 2015. Top ten European heatwaves since 1950 and their occurrence in the coming decades. *Environ. Res. Lett.* 10, 124003. <https://doi.org/10.1088/1748-9326/10/12/124003>.
- Schaller, N., Sillmann, J., Anstey, J., et al., 2018. Influence of blocking on Northern European and Western Russian heatwaves in large climate model ensembles. *Environ. Res. Lett.* 13, 054015. <https://doi.org/10.1088/1748-9326/aaba55>.
- Schumacher, D.L., Keune, J., Miralles, D.G., 2020. Atmospheric heat and moisture transport to energy- and water-limited ecosystems. *Ann. N. Y. Acad. Sci.* 1472, 123–138. <https://doi.org/10.1111/nyas.14357>.
- Seneviratne, S.I., Corti, T., Davin, E.L., et al., 2010. Investigating soil moisture–climate interactions in a changing climate: a review. *Earth Sci. Rev.* 99, 125–161. <https://doi.org/10.1016/j.earscirev.2010.02.004>.
- Serreze, M.C., Francis, J.A., 2006. The Arctic amplification debate. *Clim. Change* 76, 241–264. <https://doi.org/10.1007/s10584-005-9017-y>.
- Simpkins, G., 2017. Extreme Arctic heat. *Nat. Clim. Change* 7, 95. <https://doi.org/10.1038/nclimate3213>, 95.
- Teuling, A.J., Seneviratne, S.I., Stöckli, R., et al., 2010. Contrasting response of European forest and grassland energy exchange to heatwaves. *Nat. Geosci.* 3, 722–727. <https://doi.org/10.1038/ngeo950>.
- Thompson, D.W.J., Solomon, S., Kushner, P.J., et al., 2011. Signatures of the Antarctic ozone hole in Southern Hemisphere surface climate change. *Nat. Geosci.* 4, 741–749. <https://doi.org/10.1038/ngeo1296>.
- Vogel, M.M., Orth, R., Cheruy, F., et al., 2017. Regional amplification of projected changes in extreme temperatures strongly controlled by soil moisture-temperature feedbacks. *Geophys. Res. Lett.* 44, 1511–1519. <https://doi.org/10.1002/2016GL071235>.
- Wang, J., Chen, Y., Liao, W., et al., 2021. Anthropogenic emissions and urbanization increase risk of compound hot extremes in cities. *Nat. Clim. Change* 11, 1084–1089. <https://doi.org/10.1038/s41558-021-01196-2>.
- Wang, J., Chen, Y., Tett, S.F.B., et al., 2020a. Anthropogenically-driven increases in the risks of summertime compound hot extremes. *Nat. Commun.* 11, 528. <https://doi.org/10.1038/s41467-019-14233-8>.
- Wang, J., Feng, J., Yan, Z., et al., 2020b. Future risks of unprecedented compound heat waves over three vast urban agglomerations in China. *Earths Future* 8, e2020EF001716. <https://doi.org/10.1029/2020EF001716>.
- Wu, S., Luo, M., Zhao, R., et al., 2023. Local mechanisms for global daytime, nighttime, and compound heatwaves. *NPJ Clim. and Atmos. Sci.* 6, 1–13. <https://doi.org/10.1038/s41612-023-00365-8>.
- Yang, C.-L., Bao, J.-Z., Bi, P., et al., 2024. Association between heat and upper urinary tract stones morbidity and medical costs: a study in the subtropical humid climate zone. *Adv. Clim. Change Res.* 15, 717–724. <https://doi.org/10.1016/j.accre.2024.07.001>.
- Yuan, Y., Liao, Z., Zhou, B., et al., 2023. Unprecedented hot extremes observed in city clusters in China during summer 2022. *J. Meteorol. Res.* 37, 141–148. <https://doi.org/10.1007/s13351-023-2184-9>.
- Zhang, J., Tian, W., Chipperfield, M.P., et al., 2016. Persistent shift of the Arctic polar vortex towards the Eurasian continent in recent decades. *Nat. Clim. Change* 6, 1094–1099. <https://doi.org/10.1038/nclimate3136>.
- Zhao, C., Li, Y.-H., Tong, S., et al., 2023. Economic burden of premature deaths attributable to different heatwaves in China: a multi-site study, 2014–2019. *Adv. Clim. Change Res.* 14, 836–846. <https://doi.org/10.1016/j.accre.2023.11.003>.
- Zhou, Q.-Y., Gao, M.-N., Yang, J., et al., 2025. Future changes in population exposure to intensified heatwaves over three major urban agglomerations in China based on excess heat factor. *Adv. Clim. Change Res.* 16, 12–24. <https://doi.org/10.1016/j.accre.2024.12.009>.